

Fundamental thresholds of realistic quantum error correction circuits from classical spin models

Davide Vodola,^{1,2,*} Manuel Rispler,^{3,*} Seyong Kim,⁴ and Markus Müller^{5,6}

¹*Dipartimento di Fisica e Astronomia dell'Università di Bologna, I-40127 Bologna, Italy*

²*INFN, Sezione di Bologna, I-40127 Bologna, Italy*

³*QuTech, Delft University of Technology, Lorentzweg 1, 2628 CJ Delft, The Netherlands*

⁴*Department of Physics, Sejong University, 05006 Seoul, Republic of Korea*

⁵*Institute for Theoretical Nanoelectronics (PGI-2), Forschungszentrum Jülich, 52428 Jülich, Germany*

⁶*JARA-Institute for Quantum Information, RWTH Aachen University, 52056 Aachen, Germany*

(Dated: May 3, 2022)

Mapping quantum error correcting codes to classical disordered statistical mechanics models and studying the phase diagram of the latter has proven a powerful tool to study the fundamental error robustness and associated critical error thresholds of leading quantum error correcting codes under phenomenological noise models. In this work, we extend this mapping to admit realistic, multi-parameter faulty quantum circuits in the description of quantum error correcting codes. Based on the underlying microscopic circuit noise model, we first systematically derive the associated strongly correlated classical spin models. We illustrate this approach in detail for the example of a quantum repetition code in which faulty stabilizer readout circuits are periodically applied. Finally, we use Monte-Carlo simulations to study the resulting phase diagram of the associated interacting spin model and benchmark our results against a minimum-weight perfect matching decoder. The presented method provides an avenue to assess the fundamental thresholds of QEC codes and associated readout circuitry, independent of specific decoding strategies, and can thereby help guiding the development of near-term QEC hardware.

Introduction.—The quest to develop large-scale fault-tolerant quantum computers is a multi-disciplinary endeavour and has revealed unexpected and strong connections of quantum information theory and other disciplines such as quantum engineering in atomic, optical and solid-state systems, computer science but also classical statistical physics. Exploring such links between quantum information and classical statistical physics has been fruitful in both directions, e.g. by efficient quantum algorithms to estimate partition functions of classical spin systems [1–9], by providing effective descriptions for entanglement spreading in random circuits [10–12] or in the context of quantum error correction (QEC) and fault-tolerant quantum computing. For the latter, it has been shown that large classes of leading QEC codes [13, 14] such as the topological surface code [15, 16] and color codes [17, 18] can be mapped onto disordered classical statistical mechanics models. For the latter models, locating the phase transitions between ordered and disordered phases reveals the parameter regimes and critical error thresholds for which QEC succeeds or fails, respectively [16]. So far, however, these mappings have been largely limited to QEC codes with simple phenomenological noise models: for instance, uncorrelated [16] or weakly correlated bit and/or phase flips errors [19], phenomenological models of measurement errors in the error syndrome readout [20, 21], as well as qubit loss and leakage processes [22–26] have been considered, with recent extensions also to bosonic QEC codes [27]. Realistic modeling of experimental state-of-the-art quantum hardware [28–32], however, requires a description of failure processes at the level of the underlying quantum circuits and its components by multi-parameter circuit noise models.

In this work, we extend the QEC-statistical mechanics model mapping and apply it to realistic quantum circuit-noise

scenarios. Recently it was pointed out that for Clifford measurement circuits, correlations arising from circuit noise processes can be efficiently related to effective phenomenological models and can be used as direct input for known (but maybe sub-optimal) decoders [19, 33]. Here, we use a similar approach but perform a systematic error propagation analysis and identify emerging effective noise processes in realistic quantum circuits. Instead of direct decoding, we then derive the associated disordered classical spin model which contains correlated quenched disorder, and finally we determine its phase diagram. Thereby, here we complete a multi-step process of mapping microscopic circuit noise in realistic QEC circuitry into a classical spin model and finally obtaining the fundamental error thresholds associated with the given quantum circuit noise through investigation of the phase transition of the emergent classical spin model with quenching correlation.

We show that one can obtain and compare maximum threshold values without the need of optimal decoding and completely agnostic to specific (and generally sub-optimal) decoding strategies. This method, while not providing specific decoding protocols, opens a new avenue to assess the maximum potential of realistic QEC systems which are currently developed in a number of physical platforms, by accounting for quantum circuit level noise processes. This is particularly pressing and valuable for QEC codes because even (near-)optimal decoding is computationally hard [34], or optimal decoders are unknown/strongly dependent on the chosen QEC circuitry and details of the circuit noise models [35]. Despite the fact that significant improvements in thresholds have recently been achieved, for instance in the context of measurement circuits for high-weight stabilizers in color codes [36–38] or for recently developed flag-qubit based QEC [39–42], our method can be particularly valuable as it provides decoder-independent upper bounds on the maximally achievable thresholds against which practical (sub-

* These two authors contributed equally to the present work.

optimal decoders can then be benchmarked.

We illustrate this circuit-level QEC-statistical mechanics mapping for a one-dimensional quantum repetition code with associated stabilizer readout circuitry and a multi-parameter microscopic circuit noise model, which distinguishes between two-qubit gate errors and a number of single-qubit noise processes. Whereas this code does not allow one to correct arbitrary errors, it is currently at the focus of experimental efforts to realise repetitive QEC in the regime of beneficial error suppression for increasing code sizes [43–46]. We show that in contrast to oversimplified effective ad-hoc formulations of phenomenological noise models, new effective correlated noise processes arise, which we systematically derive and quantitatively relate to the one- and two-qubit error rates of the underlying microscopic noise model. We numerically map out the phase diagram of the resulting interacting spin model and benchmark our results against a minimum-weight perfect matching (MWPM) decoder.

We anticipate that this comparison reveals a clear and robust performance gap between efficient, though sub-optimal MWPM decoding and the fundamental upper limit as established via the statistical physics model, thereby demonstrating the viability of this complete mapping approach to identify maximal performance of QEC circuitry. Furthermore, our findings complement previous results on performance differences for purely phenomenological noise and establish that such a performance gap exists and persists over a wide range of parameters also for multi-parameter circuit noise.

Noisy quantum error correcting circuitry.—The principal idea behind quantum error correcting stabilizer codes [47] is to exploit redundancy offered by the design of the QEC code to diagnose and correct errors. The simplest code of this class is the repetition code [48, 49], which we use here in its version protecting against phase-flip errors. The code-states of the n *data* qubits D_i of this code correspond to the joint $+1$ eigenstates of the $n-1$ stabilizers $S_i = X_i \otimes X_{i+1}$ (X_i denotes a Pauli X matrix acting on qubit i), and the collection of the $n-1$ stabilizer eigenvalues form the error syndrome. The logical basis states or code words are given by the two GHZ-states $|\bar{0}/\bar{1}\rangle = (|+\rangle^{\otimes n} \pm |-\rangle^{\otimes n}) / \sqrt{2}$, with $|\pm\rangle = (|0\rangle \pm |1\rangle) / \sqrt{2}$, which make up one encoded qubit with logical operators $Z_L = \otimes_{i=0}^{n-1} Z_i$ and $X_L = X_i$ (for any i [50]). Error states are marked by having at least one non-trivial syndrome. In order to diagnose potential errors, the operators S_i are measured by coupling them to $n-1$ *ancilla* qubits. Any operation on the data qubits that does not commute with the stabilizer operators will flip the outcome of some of the Pauli measurements, such that this particular code is able to detect phase-flips Z_i , as long as they do not happen on all qubits, which would be indistinguishable from a logical phase flip Z_L . Since the stabilizer measurements are executed on the same hardware as the data qubits, they have to be treated as noisy as well, and errors in this measurement process potentially poison the measurement information. This problem can be alleviated by repeating the syndrome measurements and analysing the discrete difference in time between successive rounds – this results in another repetition code in the time domain. This yields a (1+1)-dimensional space-time *syndrome volume*, which needs to be

decoded. A key figure of merit is to identify the threshold error probability, the critical value, below which error correction is feasible, i.e. the parameter regime in which errors are suppressed exponentially with growing system size. The code performance has been studied for phenomenological noise: the code-capacity critical error threshold is $p_c = 0.5$, when the only error source are data qubit errors. The phenomenological noise threshold, where one assumes errors being injected once per round with an error rate p on both ancilla and data qubits is known to be $p_c \approx 0.11$ [51] – note that, not by accident, this is identically the threshold of the toric code with perfect measurements. The latter exactly maps onto the threshold of the repetition code with phenomenological noise, essentially trading one spatial dimension for the time dimension that is introduced by repeating the stabilizer measurements in time. Furthermore, this situation can be understood as a special case in the statistical mapping we investigate further in the present work. In contrast to these phenomenological noise models, which ignore the physical reality of the circuit the QEC code is running on, in this work we analyze a multi-parameter circuit level noise model that treats every component of the circuit as faulty, as illustrated in Fig. 1(a1).

Microscopic circuit noise processes.—Here, every single-qubit operation on the i th qubit is modeled as noisy according to a depolarizing channel (depicted as grey boxes in Fig. 1(a1)) that keeps the qubit intact with probability $1-\lambda$ and otherwise results in a random Pauli operation P_i ($P_i \in X, Y, Z$) with probability $\lambda/3$. The parameter λ can represent the error probabilities for state preparation (p_{sp}), idling, i.e. waiting while other qubits undergo operations (p_{id}), single-qubit gates (p_1) and measurements (p_m) [35, 52]. Likewise, faulty two-qubit operations (CNOT gates) are modelled by depolarizing noise that keeps the two qubits at hand intact with probability $1-p_2$ and otherwise injects any of the fifteen non-trivial two-qubit Pauli operators $P_i \otimes P_j$ ($P_i \in \mathbb{1}, X, Y, Z$ are Pauli operators acting on qubit i) with probability $p_2/15$. Single and two-qubit errors propagate through the circuit following the rules described in Fig. 1(a2). For the special case of uniform error probabilities ($p_{sp} = p_{id} = p_1 = p_m = p_2 = \lambda$) the threshold was found to lie at $\lambda \approx 0.033$ for maximum likelihood decoding [53].

Effective noise processes.—For the multi-parameter depolarizing noise model, any microscopic circuit-level error configuration will result in one of three effective error processes or combinations thereof, called error chains E in the following, with associated error probabilities per stabilizer measurement round (see Fig. 1(b1)): (i) a single-qubit phase flip error on data qubits with associated error probability p , (ii) a measurement error with probability q flipping the measurement outcome, and (iii) a correlated error flipping a data-qubit and simultaneously flipping one of the adjacent measurement outcomes, that happens with probability r . Note that these effective phase flip, measurement and correlated errors can result from multiple microscopic noise events and combinations thereof. Examples of these three effective processes are shown in Fig. 1(b1). As we derive in detail in the supplementary material [54], through combinatorial analysis based on the propagation of Pauli error generators underlying all the

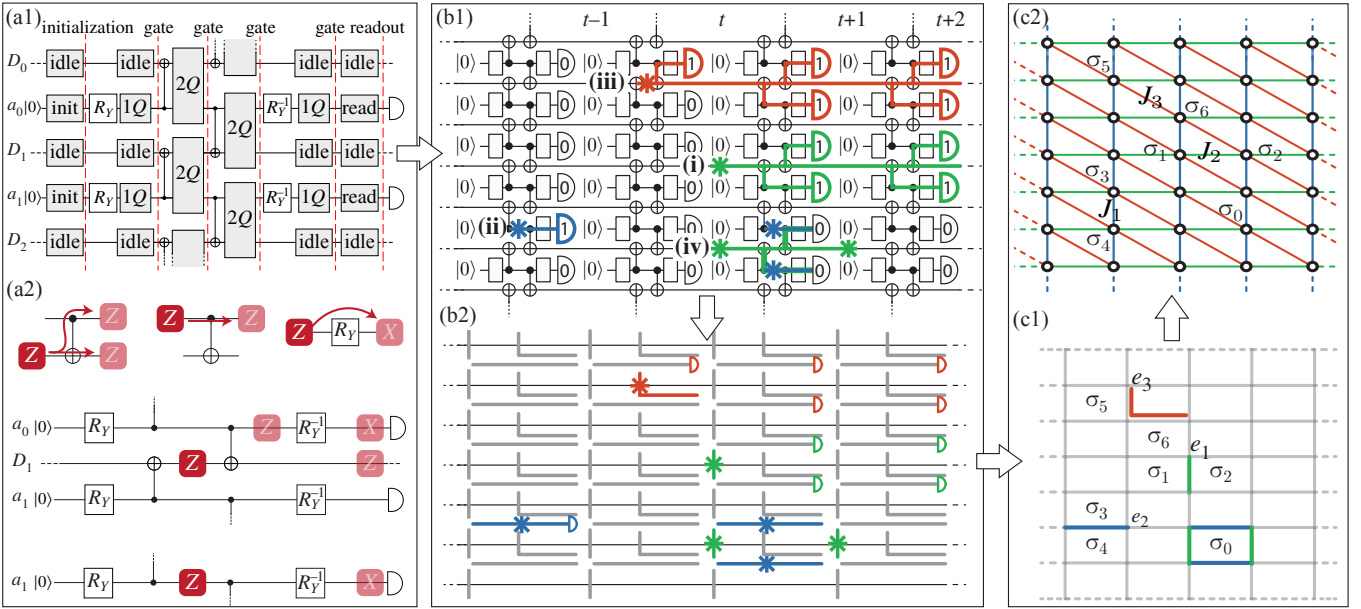


FIG. 1. (a1) One cycle of the n -qubit phase-flip repetition code with the circuit-level noise model, with the circuitry shown for an excerpt of the quantum register displaying three data qubits D_i and two ancilla qubits a_i . The white boxes labeled as R_Y (R_Y^{-1}) represent single-qubit rotations around the Y axis with an angle of $\pi/2$ ($-\pi/2$). The gray boxes labeled as idle, init, $1Q$ and $2Q$ are depolarizing noise channels describing faulty events occurring during idling, state preparation, single-qubit and CNOT gates, respectively. (a2) (Top row) Examples of error propagation through the CNOT gates and the single-qubit rotations R_Y : a Z error on the target qubit propagates to the control qubit, but Z errors do not propagate from the control qubit to the target qubit; a Z error is transformed into an X error through R_Y . (Center row) A Z error occurring between two CNOTs on the data qubit D_1 propagates also to the upper ancilla a_0 , where it eventually shows up in the measurement. (Bottom row) A Z error occurring between the rotations R_Y on the ancilla results in a measurement error. (b1) Four measurement cycles of the repetition code showing the error propagation according to the processes shown in (a2), and the affected ancilla qubits. (i) A data qubit error (green asterisk) propagates according to the green path and affects two ancilla qubits at every subsequent measurement step. (ii) A measurement error (blue asterisk), which affects a single ancilla measurement. (iii) An error happening between the CNOT gates of a data qubit (red asterisk) propagates according to the red path and affects only one ancilla at step t and two ancilla qubits at the subsequent measurement steps. (iv) A space-time equivalence given by two qubit errors and two measurement errors that does not show up in any ancilla read out. (b2) Error graph generated by the physical errors in panel (b1). Positions where qubit, measurement and correlated data phase-flip and measurement errors can happen are represented by vertical, horizontal and L-shaped edges, respectively. Colored semicircles represent the ancilla qubits that have been triggered by an error event. From this graph we derive the fundamental error events that determine the couplings of the statistical mechanics Hamiltonian (panels (c1)-(c2)) and the syndrome volume which is the input for the MWPM decoder. (c1) Fundamental errors e_1, e_2, e_3 generated by the error processes (i)-(iii) and equivalences σ_ℓ . (c2) Lattice of equivalences σ_ℓ showing the couplings J_1 (vertical blue links), J_2 (horizontal green links), J_3 (diagonal red links) of the Hamiltonian of Eq. (2).

various circuit noise processes and factorizing and rearranging the effective error channel(s) and resultant Pauli transfer matrices, we can express an arbitrary Pauli circuit noise model in terms of the three effective error rates p, q and r :

$$\begin{aligned}
 p &= \frac{1}{2} \left[1 - \left(1 - \frac{16p_2}{15} \right) \left(1 - \frac{4p_{\text{id}}}{3} \right)^4 \right] \\
 q &= \frac{1}{2} \left[1 - \left(1 - \frac{16p_2}{15} \right) \left(1 - \frac{4p_1}{3} \right)^2 \left(1 - \frac{4p_{\text{sp}}}{3} \right) \left(1 - \frac{4p_{\text{m}}}{3} \right) \right] \\
 r &= \frac{8}{15} p_2.
 \end{aligned} \tag{1}$$

We can gather the error events from the microscopic processes happening on the realistic circuit (Fig. 1(b1)) in the error graph of Fig. 1(b2): here the vertical, horizontal and L-shaped lines indicate the possible positions where a data-qubit

(i), a measurement (ii) or a correlated error (iii) event can be found. The colored links indicate the positions where an error has occurred, while the colored semicircles indicate the stabilizers that are triggered by the respective error event.

In the following, the error graph is used for two purposes: on the one hand, it is the basis to construct the types of interactions that appear in the classical statistical mechanics Hamiltonian (Fig. 1(c1)), and on the other hand it gives rise to the syndrome volume as input for the MWPM decoder.

From the error graph, we can visualize the error processes by introducing the lattice in Fig. 1(c1) where vertical links represent data qubits and horizontal links are measurement steps. The three error processes (i)-(iii) define the fundamental errors events e_1, e_2, e_3 shown in Fig. 1(c1): the error e_1 is generated by a single qubit phase flip error (i) or by a combination of a measurement error (ii) and a correlated error (iii) with probability $\text{Pr}(e_1) = p(1-q)(1-r) + (1-p)qr$. The error e_2 is generated by a measurement error (ii) or by a combina-

tion of a single qubit phase flip error (i) and a correlated error (iii) and has probability $\Pr(e_2) = q(1-p)(1-r) + rp(1-q)$. Finally the error e_3 is generated by a correlated error (iii) or by a combination of a single qubit phase flip error (i) and a measurement error (ii) and has probability $\Pr(e_3) = r(1-p)(1-q) + pq(1-r)$. These fundamental errors combine and form error chains E that can be parameterized by introducing binary variables $h_\ell, v_\ell \in \{\pm 1\}$ for each link ℓ of the lattice. The variables $h_\ell (v_\ell)$ take a negative value -1 if the horizontal (vertical) link ℓ belongs to the error E .

Statistical mechanics model.—Mapping an error model into a statistical mechanics Hamiltonian allows us to compute the probability $\Pr(\bar{E})$ of the class \bar{E} made by all the errors that differ from a reference (candidate) error chain E by a so-called *space-time equivalence* [16, 19]: A space-time equivalence $\hat{\sigma}$ (called equivalence in the following) is a trivial sequence of errors that are not detected by the stabilizers and thus produce the same space-time syndrome volume. For the phase flip code, the equivalences are given by the action of a single phase flip on a qubit D_i at a measurement step t , followed by two measurement errors on the ancilla qubits of the stabilizer S_i adjacent to D_i and a last phase flip error on D_i before the measurement step $t+2$ (see (iv) in Fig. 1(b1)). We can associate a classical Ising spin σ to each of the equivalences (e.g. σ_0 in Fig. 1(c1)) such that a spin configuration with $\sigma = -1$ effectively describes the error $E' = E\hat{\sigma}$ that differs from the reference error chain E by the equivalence $\hat{\sigma}$. This means that once we fix E , sampling over all the possible spin configurations is equivalent to sampling over all possible errors E' in the class \bar{E} and the probability of the class \bar{E} can be written as $\Pr(\bar{E}) = \sum_{\{\hat{\sigma}\}} \Pr(E\hat{\sigma})$. Given an error E and the equivalences, one can also define the two classes $\overline{EO_L}$ for each logical operator $O_L = Z_L, X_L$ and compute the relative probabilities $\Pr(\overline{EO_L})$ by the statistical mechanics mapping. Comparing $\Pr(\bar{E})$ and $\Pr(\overline{EO_L})$ allows us to determine if the error is correctable which occurs if $\Pr(\bar{E}) > \Pr(\overline{EO_L})$ for any logical operator.

Given the reference error E described by $h_\ell \in \{\pm 1\}$ and $v_\ell \in \{\pm 1\}$ and the set of equivalences $\{\sigma\}$, the probability of the error E' can be written as $\Pr(E') = \exp[-\beta H_E(\sigma)]$ where

$$H_E(\sigma) = - \sum_{\ell \uparrow \ell'} J_1 h_\ell \sigma_\ell \sigma_{\ell'} - \sum_{\ell \leftrightarrow \ell'} J_2 v_\ell \sigma_\ell \sigma_{\ell'} - \sum_{\ell \nwarrow \ell'} J_3 h_\ell v_\ell \sigma_\ell \sigma_{\ell'} \quad (2)$$

is an Ising Hamiltonian with correlated quenched disorder. The couplings J_1, J_2, J_3 and the inverse temperature β are fixed from the error model describing E by the so-called Nishimori conditions $\Pr(e_j) = \exp[-\beta H_{e_j}(\{+1\})]$ for $j = 1, 2, 3$ where for the Hamiltonian H_{e_j} , we consider the state where all the classical spins are $+1$ (see the supplementary material [54]). The type of interactions (ferromagnetic or antiferromagnetic) is given by the signs of v_ℓ and h_ℓ that are fixed by the reference error E . In the first sum of the r.h.s. of Eq. (2), σ_ℓ and $\sigma_{\ell'}$ are the spins horizontally adjacent to the link ℓ (e.g. spins σ_1 and σ_2 in Fig. 1(c1)); in the second sum, σ_ℓ and $\sigma_{\ell'}$ are the spins vertically adjacent to the link ℓ (e.g. spins σ_3 and σ_4 in Fig. 1(c1)); in the third sum, σ_ℓ and $\sigma_{\ell'}$ are the two spins adjacent to the two arms of the L-shaped error e_3 (e.g. spins

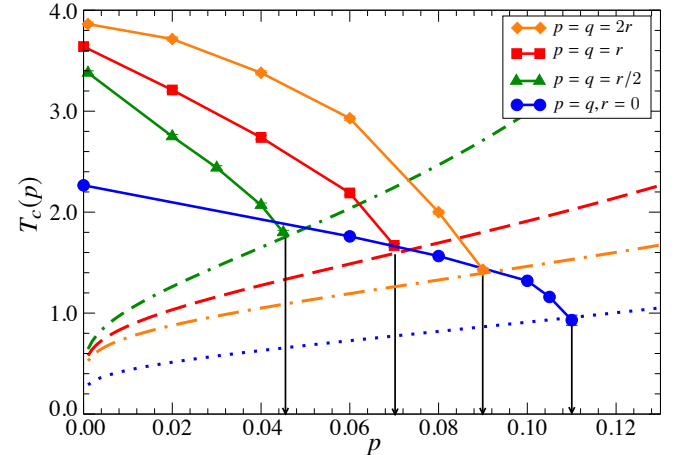


FIG. 2. Phase diagram of the random bond Ising model for four different quenched disorder cases: (I) $p = q = 2r$ (orange diamonds), (II) $p = q = r$ (red squares), (III) $p = q = r/2$ (green triangles), (IV) $p = q, r = 0$ (square lattice, blue circles). The points for each case represent the critical temperature T_c for the given disorder configuration. Solid lines are a guide to the eye, and dashed lines correspond to the Nishimori lines for each case. The black solid vertical lines indicate the locations of the largest p simulated that exhibits critical behavior. Note that the blue data point at $p = 0.11$ is obtained with 10 times longer MC runs than all the other points and the errors in most of data points are smaller than the size of the symbol.

σ_5 and σ_6 in Fig. 1(c1)). A similar Hamiltonian has been analyzed in [19] in the context of a surface code with spatially correlated phenomenological noise, whereas here the Hamiltonian (2) arises from a multi-parameter circuit noise model.

Numerical results.—Mapping the quantum code to the Hamiltonian (2) allows us to access the error robustness of the QEC code from the thermodynamic properties of $H_E(\sigma)$ [16]. In particular, the error threshold separating the correctable from non-correctable parameter regime of the code corresponds to the phase transition point between the ordered and the disordered phases of $H_E(\sigma)$. We determine this transition from Monte Carlo (MC) simulations and a scaling analysis of the two-body spin correlation length for various disorder strengths (see the supplementary material [54] for details). To this end, it is convenient to transform the lattice in Fig. 1(c1) into the triangular one of Fig. 1(c2) where the classical spins (white circles) reside on the vertices and the couplings J_1, J_2, J_3 are represented by the vertical (blue), horizontal (green) and diagonal (red) links, respectively.

In Fig. 2, we show the phase diagram obtained from MC simulations for three choices of parameter settings for the correlated case (I) $p = q = 2r$, (II) $p = q = r$, (III) $p = q = r/2$, and for the uncorrelated case (IV) $p = q$ and $r = 0$, the latter reducing to a random bond Ising model on a square lattice. We find that in order of increasing correlated error strength r , the thresholds decrease to $p_c(\text{I}) = 0.0925(25)$, $p_c(\text{II}) = 0.0725(25)$, $p_c(\text{III}) = 0.0475(25)$ from the uncorrelated threshold $p_c(\text{IV}) = 0.110(5)$. Near the Nishimori lines, longer MC runs are required to locate p_c and T_c more accurately. The error in p_c is determined within the present MC

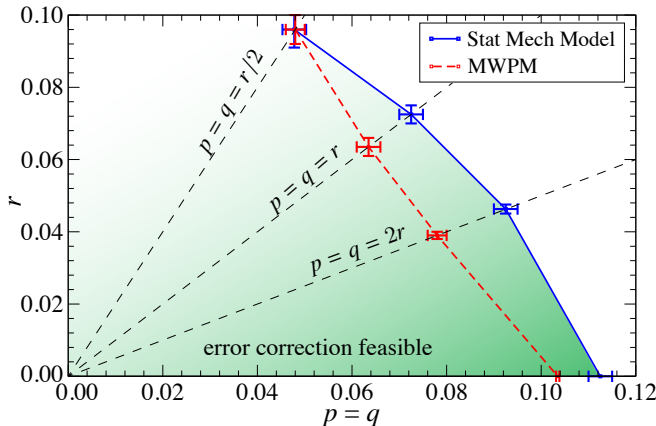


FIG. 3. Threshold probabilities from the statistical mechanics model (blue points, solid line) and the MWPM decoder (red points, dashed line). The region where the MWPM decoder finds the code correctable lies within the ordered region of the statistical mechanics model. The ordered region represents the fundamental region independent on any decoding scheme where the repetition code can be corrected with success. Lines connecting the points are a guide to the eye.

statistics. The details of the MC simulation can be found in the supplementary material [54].

Minimum weight matching decoder.—MWPM is efficient thanks to Edmond’s Blossom algorithm [55]. Owing to the exact mapping of circuit noise to the effective noise rates, it suffices to simulate effective noise rates on data qubits and the syndrome, allowing for efficient simulation of the QEC code. We sample from the error distributions, recording both errors and syndrome. We then present the syndrome to the MWPM decoder. If the resulting decoder decision agrees with the recorded error history, we declare logical correction success, otherwise logical correction failure. We estimate logical failure rates by sampling for varying system size and error rate(s). This enables us to extract threshold values, which signify the critical value below which increasing the system size is beneficial to the logical success rate. The thresholds extracted via MWPM provide lower bounds to the thresholds obtained through the statistical mechanics mapping since they correspond to a decoding decision that is not necessarily optimal: MWPM looks for the likeliest error explaining the observed syndrome, which in the statistical mechanics mapping can be viewed as minimizing the energy as opposed to the free energy [16]. In order to be able to assign weights to matchings, we need to devise the corresponding metric, which is given by the minimum over the (weighted) Manhattan distance on the three sublattices of the triangular lattice. We defer the reader to the supplementary material for a detailed derivation of the error weight metric and the general MWPM decoding strategy.

Discussion.—In Fig. 3 we show the phase diagram with the thresholds from Monte Carlo simulations (blue points, solid line) and from MWPM (red points, dotted line). The figure demonstrates that the region where MWPM successfully decodes lies within error bars inside the fundamental region of

correctability determined with the statistical mechanics mapping. This demonstrates a finite interval between MWPM and a higher fundamental threshold that could be achieved by improving the decoding strategy. To connect the phase diagram to experimental situations, let us discuss the relative strength of r and its meaning. First off, p and q both are typically dominated by similar error processes that for many qubit platforms are of comparable error rate quality, hence we set $p = q$ for simplicity. On top of that, we then dial up the strength of r . The known case $r = 0$ reduces to the phenomenological case without correlated errors, which would correspond to a perfect two-qubit gate ($p_2 = 0$). Increasing r to $r = p/2 = q/2$ corresponds to $p_2 = 5p_1 + O(p_1^2)$, which is roughly compatible with the two-qubit gate being an order of magnitude worse than single-qubit operations (error rate or infidelity) observed in many experimental realizations [28, 32, 46, 56]. Going beyond that, $r = p = q$ corresponds to p_2 being the dominant error source, where all other error sources are negligible ($p_{sp} = p_{id} = p_1 = p_m = 0$). The case $r = 2p = 2q$ goes beyond the depolarizing noise model that is behind Eq. (1): not only is the two-qubit gate the only error source, it furthermore specifically produces the errors leading to the r type instead of p and q , which goes beyond the circuit-level noise paradigm and would be described by an asymmetric depolarizing noise channel biased towards r . While this does not seem typical, it is not beyond reason to imagine a two-qubit gate producing biased noise. Finally, let us mention that the case of pure r errors ($p = q = 0$) corresponds to a situation where we can perfectly trust the syndrome information if we interpret it correctly, akin to a repetition code with perfect measurements (which entails a threshold approaching 0.5 asymptotically). Having this intuition for the meaning of the parameter ranges in mind, we see that the experimentally most relevant region $r \neq p = q$ is the region where we also see a separation between the MWPM and the fundamental threshold. The separation seems to become narrower for higher contributions of r , which we can connect to the expectation in the extreme case of pure r error. Since this corresponds to a “skewed” repetition code with perfect measurements, we know that the latter can be decoded perfectly with MWPM, since there are no degeneracies left, which agrees with the narrowing separation when r becomes dominant. To complement the interpretation of the phase-diagram, we can also read it in the following way: the estimated thresholds for ideal decoding and MWPM respectively in case of $p = q = 2r$ correspond to single-qubit errors $p_1 \approx 0.02$ (ideal decoding) vs. 0.017 (MWPM decoding) and the two-qubit error rate $p_2 \approx 0.087$ (ideal) vs. 0.074 (MWPM). In the case $p = q = r$ the threshold is $p_2 \approx 0.14$ (ideal) vs. 0.12 (MWPM).

Interestingly, in a recent experimental realization of the phase-flip code [46], the authors report that the circuit errors are well described by Pauli errors and furthermore specify the corresponding error rates. Casting these experimentally obtained error rates into Eq. (1), we find that they correspond to the effective error rates $p = 0.032$, $q = 0.0285$ and $r = 0.0035$, which is in excellent agreement with the observation that this experiment is thoroughly in the error-suppression regime.

Conclusions and Outlook.—In this work, we have mapped

a realistic multi-parameter circuit noise model into a classical statistical mechanics model with quenched disorder and determined the associated fundamental error thresholds. We have benchmarked this technique for the case of a phase flip repetition code and systematically compared our findings with results from MWPM decoding. The principles of the presented technique can be applied to more complex complete QEC codes, to determine fundamental, i.e. decoder-independent thresholds for circuit-noise models of leading QEC codes, including the surface and color code, as well as concatenated codes. Here, we anticipate that as the code circuitry becomes more complex, it will be necessary to include more types of effective noise processes, which in turn will give rise to new statistical mechanics models with even richer interaction and disorder properties. It will also be interesting to extend the mapping technique to non-Clifford dynamics, as well as to temporally or spatially correlated circuit-level noise processes to allow for the study of an even broader class of models of state-of-the-art quantum processors.

Acknowledgments.—We thank B. Lucini, C. Chubb and S. Flammia for useful discussions and B.M. Terhal, E. Fiorelli and P. Pieri for their feedback on the manuscript. SK is supported by the National Research Foundation of Korea under grant NRF-2018R1A2A2A05018231 funded by the Korean government (MEST) and in part by NRF-2008-000458. MM acknowledges support by the ERC Starting Grant QNets Grant Number 804247, the EU H2020-FETFLAG-2018-03 under Grant Agreement number 820495, by US A.R.O. through Grant No. W911NF-21-1-0007, and by the Office of the Director of National Intelligence (ODNI), Intelligence Advanced Research Projects Activity (IARPA), via US ARO Grant number W911NF-16-1-0070. All statements of fact, opinions or conclusions contained herein are those of the authors and should not be construed as representing the official views or policies of ODNI, the IARPA, or the US Government. MR is supported by ERC grant EQEC No. 682726. MR would like to thank D.P. DiVincenzo for generously providing access to computing facilities.

[1] D. A. Lidar and O. Biham, Simulating Ising spin glasses on a quantum computer, *Phys. Rev. E* **56**, 3661 (1997).

[2] R. D. Somma, C. D. Batista, and G. Ortiz, Quantum approach to classical statistical mechanics, *Phys. Rev. Lett.* **99**, 030603 (2007).

[3] M. Van den Nest, W. Dür, and H. J. Briegel, Classical spin models and the quantum-stabilizer formalism, *Phys. Rev. Lett.* **98**, 117207 (2007).

[4] J. Geraci and D. A. Lidar, On the exact evaluation of certain instances of the Potts partition function by quantum computers, *Commun. Math. Phys.* **279**, 735 (2008).

[5] G. De las Cuevas, W. Dür, H. J. Briegel, and M. A. Martin-Delgado, Unifying all classical spin models in a lattice gauge theory, *Phys. Rev. Lett.* **102**, 230502 (2009).

[6] G. De las Cuevas, W. Dür, M. V. den Nest, and M. A. Martin-Delgado, Quantum algorithms for classical lattice models, *New J. Phys.* **13**, 093021 (2011).

[7] Y. Xu, G. De las Cuevas, W. Dür, H. J. Briegel, and M. A. Martin-Delgado, The U(1) lattice gauge theory universally connects all classical models with continuous variables, including background gravity, *J. Stat. Mech-Theory E* **2011**, P02013 (2011).

[8] G. De las Cuevas and T. S. Cubitt, Simple universal models capture all classical spin physics, *Science* **351**, 1180 (2016).

[9] M. H. Zarei and A. Montakhab, Dual correspondence between classical spin models and quantum Calderbank-Shor-Steane states, *Phys. Rev. A* **98**, 012337 (2018).

[10] Y. Li and M. P. A. Fisher, Statistical mechanics of quantum error-correcting codes (2020), [arXiv:2007.03822 \[quant-ph\]](https://arxiv.org/abs/2007.03822).

[11] A. Nahum, S. Vijay, and J. Haah, Operator spreading in random unitary circuits, *Phys. Rev. X* **8**, 021014 (2018).

[12] T. Zhou and A. Nahum, Emergent statistical mechanics of entanglement in random unitary circuits, *Phys. Rev. B* **99**, 174205 (2019).

[13] B. M. Terhal, Quantum error correction for quantum memories, *Rev. Mod. Phys.* **87**, 307 (2015).

[14] D. A. Lidar and T. A. Brun, eds., *Quantum Error Correction* (Cambridge University Press, Cambridge, England, 2013).

[15] A. Kitaev, Fault-tolerant quantum computation by anyons, *Ann. Phys.* **303**, 2 (2003).

[16] E. Dennis, A. Kitaev, A. Landahl, and J. Preskill, Topological quantum memory, *J. Math. Phys.* **43**, 4452 (2002).

[17] H. Bombin and M. A. Martin-Delgado, Topological quantum distillation, *Phys. Rev. Lett.* **97**, 180501 (2006).

[18] H. Bombin and M. A. Martin-Delgado, Topological computation without braiding, *Phys. Rev. Lett.* **98**, 160502 (2007).

[19] C. T. Chubb and S. T. Flammia, Statistical mechanical models for quantum codes with correlated noise (2019), [arXiv:1809.10704 \[quant-ph\]](https://arxiv.org/abs/1809.10704).

[20] T. Ohno, G. Arakawa, I. Ichinose, and T. Matsui, Phase structure of the random-plaquette Z_2 gauge model: accuracy threshold for a toric quantum memory, *Nucl. Phys. B* **697**, 462 (2004).

[21] R. S. Andrist, H. G. Katzgraber, H. Bombin, and M. A. Martin-Delgado, Tricolored lattice gauge theory with randomness: fault tolerance in topological color codes, *New J. Phys.* **13**, 83006 (2011).

[22] T. C. Ralph, A. J. F. Hayes, and A. Gilchrist, Loss-tolerant optical qubits, *Phys. Rev. Lett.* **95**, 100501 (2005).

[23] T. M. Stace, S. D. Barrett, and A. C. Doherty, Thresholds for Topological Codes in the Presence of Loss, *Phys. Rev. Lett.* **102**, 200501 (2009).

[24] T. M. Stace and S. D. Barrett, Error correction and degeneracy in surface codes suffering loss, *Phys. Rev. A* **81**, 022317 (2010).

[25] D. Vodola, D. Amaro, M. A. Martin-Delgado, and M. Müller, Twins percolation for qubit losses in topological color codes, *Phys. Rev. Lett.* **121**, 060501 (2018).

[26] D. Amaro, J. Bennett, D. Vodola, and M. Müller, Analytical percolation theory for topological color codes under qubit loss, *Phys. Rev. A* **101**, 032317 (2020).

[27] C. Vuillot, H. Asasi, Y. Wang, L. P. Pryadko, and B. M. Terhal, Quantum error correction with the toric Gottesman-Kitaev-Preskill code, *Phys. Rev. A* **99**, 032344 (2019).

[28] C. D. Bruzewicz, J. Chiaverini, R. McConnell, and J. M. Sage, Trapped-ion quantum computing: Progress and challenges, *Applied Physics Reviews* **6** (2019).

[29] M. Kjaergaard, M. E. Schwartz, J. Braumüller, P. Krantz, J. I.-J. Wang, S. Gustavsson, and W. D. Oliver, Superconducting qubits: Current state of play, *Annual Review of Condensed Matter Physics* **11**, 369 (2020).

[30] M. Saffman, Quantum computing with atomic qubits and Rydberg interactions: progress and challenges, *Journal of Physics B: Atomic, Molecular and Optical Physics* **49**, 202001 (2016).

[31] S. Pezzagna and J. Meijer, Quantum computer based on color centers in diamond, *Applied Physics Reviews* **8**, 011308 (2021).

[32] A. Chatterjee, P. Stevenson, S. De Franceschi, A. Morello, N. P. de Leon, and F. Kuemmeth, Semiconductor qubits in practice, *Nat. Rev. Phys.* **3**, 157 (2021).

[33] L. P. Pryadko, On maximum-likelihood decoding with circuit-level errors, *Quantum* **4**, 304 (2020), 1909.06732v4.

[34] P. Iyer and D. Poulin, Hardness of Decoding Quantum Stabilizer Codes, *IEEE Trans. Inf. Theory* **61**, 5209 (2015).

[35] A. M. Stephens, Fault-tolerant thresholds for quantum error correction with the surface code, *Phys. Rev. A* **89**, 022321 (2014).

[36] D. Wang, A. Fowler, C. Hill, and L. Hollenberg, Graphical algorithms and threshold error rates for the 2d color code, *Quant. Inf. Comp* **10**, 780 (2010).

[37] A. J. Landahl, J. T. Anderson, and P. R. Rice, Fault-tolerant quantum computing with color codes (2011), arXiv:1108.5738 [quant-ph].

[38] M. E. Beverland, A. Kubica, and K. M. Svore, The cost of universality: A comparative study of the overhead of state distillation and code switching with color codes (2021), arXiv:2101.02211 [quant-ph].

[39] R. Chao and B. Reichardt, Fault-tolerant quantum computation with few qubits, *npj Quantum Information* **4** (2017).

[40] C. Chamberland and M. E. Beverland, Flag fault-tolerant error correction with arbitrary distance codes, *Quantum* **2**, 53 (2018).

[41] C. Chamberland, A. Kubica, T. J. Yoder, and G. Zhu, Triangular color codes on trivalent graphs with flag qubits, *New Journal of Physics* **22**, 023019 (2020).

[42] C. Chamberland and K. Noh, Very low overhead fault-tolerant magic state preparation using redundant ancilla encoding and flag qubits, *npj Quantum Information* **6** (2020).

[43] P. Schindler, J. T. Barreiro, T. Monz, V. Nebendahl, D. Nigg, M. Chwalla, M. Hennrich, and R. Blatt, Experimental repetitive quantum error correction, *Science* **332**, 1059 (2011).

[44] G. Waldherr *et al.*, Quantum error correction in a solid-state hybrid spin register, *Nature* **506**, 204 (2014).

[45] J. Kelly *et al.*, State preservation by repetitive error detection in a superconducting quantum circuit, *Nature* **519**, 66 (2015).

[46] Z. Chen *et al.*, Exponential suppression of bit or phase flip errors with repetitive error correction (2021), arXiv:2102.06132 [quant-ph].

[47] D. Gottesman, *Stabilizer codes and quantum error correction*, Ph.D. thesis, California Institute of Technology (1997).

[48] S. J. Devitt, W. J. Munro, and K. Nemoto, Quantum error correction for beginners, *Reports on Progress in Physics* **76**, 076001 (2013).

[49] M. A. Nielsen and I. L. Chuang, *Quantum Computation and Quantum Information* (Cambridge University Press, 2000).

[50] Due to the Pauli-X-operator being unencoded this does not comprise a full encoded quantum bit: X -errors are completely invisible to the syndrome and neither suppressed nor correctable. Nevertheless repetition codes appear at many places in (quantum) error correction. One can even view e.g. the surface code as a product of two repetition codes, cf [57].

[51] A. Honecker, M. Picco, and P. Pujol, Universality Class of the Nishimori Point in the 2D $\pm J$ Random-Bond Ising Model, *Phys. Rev. Lett.* **87**, 047201 (2001).

[52] R. Raussendorf and J. Harrington, Fault-Tolerant Quantum Computation with High Threshold in Two Dimensions, *Phys. Rev. Lett.* **98**, 190504 (2007).

[53] M. Rispler, P. Cerfontaine, V. Langrock, and B. M. Terhal, Towards a realistic GaAs-spin qubit device for a classical error-corrected quantum memory, *Phys. Rev. A* **102**, 022416 (2020).

[54] See the Supplemental Material for (1) the derivation of the parameters of the noise model; (2) the derivation of the statistical mechanical Hamiltonian; (3) the details on the Monte Carlo simulations; (4) the details on the minimum-weight-perfect-matching decoder. The Supplemental Material includes Refs. [16, 19, 58–64].

[55] J. Edmonds, Paths, trees, and flowers, *Canadian Journal of Mathematics* **17**, 449 (1965).

[56] W. Huang *et al.*, Fidelity benchmarks for two-qubit gates in silicon, *Nature* **569**, 532 (2019).

[57] J.-P. Tillich and G. Zémor, Quantum LDPC Codes With Positive Rate and Minimum Distance Proportional to the Square Root of the Blocklength, *IEEE Trans. Inf. Theory* **60**, 1193 (2013).

[58] D. Greenbaum, Introduction to quantum gate set tomography (2015), arXiv:1509.02921 [quant-ph].

[59] M. Palassini and S. Caracciolo, Universal finite-size scaling functions in the 3D Ising spin glass, *Phys. Rev. Lett.* **82**, 5128 (1999).

[60] N. Metropolis, A. W. Rosenbluth, M. N. Rosenbluth, A. H. Teller, and E. Teller, Equation of state calculations by fast computing machines, *The Journal of Chemical Physics* **21**, 1087 (1953).

[61] R. H. Swendsen and J.-S. Wang, Replica Monte Carlo simulation of spin-glasses, *Phys. Rev. Lett.* **57**, 2607 (1986).

[62] D. J. Earl and M. W. Deem, Parallel tempering: Theory, applications, and new perspectives, *Phys. Chem. Chem. Phys.* **7**, 3910 (2005).

[63] A. Hagberg, D. A. Schult, and P. J. Swart, Exploring network structure, dynamics, and function using networkx, in *Proceedings of the 7th Python in Science Conference*, edited by G. Varoquaux, T. Vaught, and J. Millman (Pasadena, CA USA, 2008) pp. 11 – 15.

[64] D. Wang, A. Fowler, A. Stephens, and L. Hollenberg, Threshold error rates for the toric and planar codes, *Quant. Inf. Comp* **10**, 456 (2010).

**Supplemental Material to
“Fundamental thresholds of realistic quantum error correction circuits from classical spin models”**

In this supplemental material we present technical details that were omitted in the main text. In particular, in Sec. I we derive the parameters of the noise model arising from the faulty microscopic circuit implementing the stabilizer read-out for the quantum repetition code. In Sec. II we derive the statistical mechanical Hamiltonian that is induced by the noise model presented in the preceding section. In Sec. III we give details on the Monte Carlo simulations for finding the phase transition lines of the statistical mechanical Hamiltonian. Finally, in Sec. IV we provide details on the minimum-weight-perfect-matching (MWPM) decoder we use to benchmark the results of the Monte Carlo simulations.

I. EFFECTIVE ERROR MODEL FROM CIRCUIT LEVEL NOISE

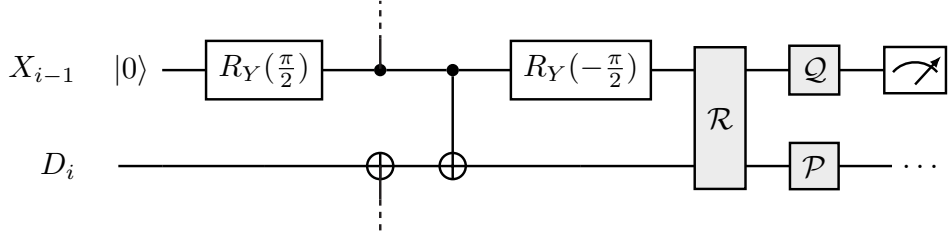


FIG. S1. Cutout of one ancilla and one data qubit of the QEC circuit. All noise contributions of the circuit-level noise model (see Fig. 1(a) of the main text) can be merged into the three channels \mathcal{P} , \mathcal{Q} and \mathcal{R} . The effective error rates are given in Eq. (S4).

Circuit-level noise in general, by definition, introduces noise channels at all locations inside the circuit. However for the given QEC code, it is possible to rewrite the noise model by exploiting equivalences of errors, arriving at a much simpler noise model (while keeping the mapping exact). Let us establish these equivalences as follows: on a data qubit, observe that X -errors do not affect the syndrome, hence for the purposes of decoding $X \sim \mathbb{1}$ and thus also $Y \sim Z$. On ancilla qubits, the situation is similar, except that the intermediate rotations $R_Y(\pm\pi/2)$ flip the relevant error: at initialization and read-out, only X -errors are relevant, Z does neither alter the initialization state nor the readout in the computational basis. Between the rotation gates $R_Y(\pm\pi/2)$, the roles are reversed and only Z is relevant. This immediately lets us move all single-qubit channels to one side, since all noise channels commute (Pauli channels commute) and the Z -errors commute past the control of the CNOT. Similarly, the data qubit single noise channels can be collected into four consecutive single qubit noise channels. Turning to the two-qubit error channels, let us observe that by the equivalence of errors there are four possible distinct errors arising from the two-qubit depolarizing channel: $\mathbb{1}\mathbb{1}$, $\mathbb{1}Z$, $Z\mathbb{1}$ and ZZ (omitting the tensor product symbol). There is a single new phenomenon encoded here: looking at the earlier CNOT noise channel, observe that ZZ is equivalent to a simple data qubit error that would have preceded the CNOT and $\mathbb{1}Z$ (data-ancilla) is equivalent to a simple measurement error, $Z\mathbb{1}$ generates a new syndrome phenomenon, which we call an r -type error. The effect of the second two-qubit noise channel is the same, just the roles of the terms being permuted. Assuming a depolarizing probability p_2 of the CNOT gate, defining the operators $P = \mathbb{1} \otimes Z$, $Q = X \otimes \mathbb{1}$ and $R = X \otimes Z = P \cdot Q$ and using hats for superoperator notation $\hat{M}(\rho) := M\rho M^\dagger$ we thus have

$$\mathcal{N}_{2qubit} = \left(1 - \frac{12p_2}{15}\right)\hat{\mathbb{1}} + \frac{4p_2}{15}(\hat{P} + \hat{Q} + \hat{R}) \quad (\text{S1})$$

This channel is a mixture of three error events, which we would like to factorize into independent channels. Remarkably, we can make the ansatz of a product of three channels and solve for their error rates.

$$(\mathcal{N}_{2qubit})^2 = [(1 - \lambda_p)\hat{\mathbb{1}} + \lambda_p\hat{P}] \cdot [(1 - \lambda_q)\hat{\mathbb{1}} + \lambda_q\hat{Q}] \cdot [(1 - \lambda_r)\hat{\mathbb{1}} + \lambda_r\hat{R}] \quad (\text{S2})$$

Note that the square means applying the channel twice, which comes from the fact that we have two two-qubit noise channels acting subsequently, both of the form S1. By symmetry of Eq. (S1), the three rates must be equal, they turn out to be $\lambda_r = \lambda_p = \lambda_q = \frac{8}{15}p_2$. For the r -type error we are done, but for the effective single-qubit channels \mathcal{P} and \mathcal{Q} , it remains to incorporate the four contributions from the single-qubit error channels. This is straightforward in the Pauli-transfer-matrix (PTM) representation [S1], where we characterize a channel \mathcal{E} by the matrix $R_{ij} = \frac{1}{d}\text{tr}(P_i\mathcal{E}(P_j))$ with $i \in \{0, 1, 2, 3\}$. The strength of this representation is that here the action of a sequence of channels is simply given by matrix multiplication of their PTMs. The PTM of a bit-flip

channel is

$$\hat{\mathcal{E}} = (1 - \gamma)\hat{\mathbb{1}} + \gamma\hat{X} \cong R_{\mathcal{E}} = \begin{pmatrix} 1 & 0 & 0 & 0 \\ 0 & 1 & 0 & 0 \\ 0 & 0 & 1 - 2\gamma & 0 \\ 0 & 0 & 0 & 1 - 2\gamma \end{pmatrix} \quad (\text{S3})$$

and furthermore it is evident that composing bit-flip channels results in a new bit-flip channel, such that we can read off the error rate from computing one of the non-trivial entries on the diagonal. This results in $\mathcal{P} = (1 - p)\hat{\mathbb{1}} + p\hat{P}$, $\mathcal{Q} = (1 - q)\hat{\mathbb{1}} + q\hat{Q}$ and $\mathcal{R} = (1 - r)\hat{\mathbb{1}} + r\hat{R}$ with

$$\begin{aligned} p &= \frac{1}{2} \left[1 - \left(1 - \frac{16p_2}{15} \right) \left(1 - \frac{4p_{\text{id}}}{3} \right)^4 \right] \\ q &= \frac{1}{2} \left[1 - \left(1 - \frac{16p_2}{15} \right) \left(1 - \frac{4p_1}{3} \right)^2 \left(1 - \frac{4p_{\text{sp}}}{3} \right) \left(1 - \frac{4p_{\text{m}}}{3} \right) \right] \\ r &= \frac{8}{15}p_2. \end{aligned} \quad (\text{S4})$$

These are the three channels depicted in Fig. S1. Let us comment on the structure of these expressions: we recover the standard circuit-level noise by setting $p_2 = p_{\text{id}} = p_{\text{m}} = p_1 = p_{\text{sp}} = \lambda$. In that case, in leading order in λ we recover $r/p = 1/6$, which can be understood also by simply counting the number of locations weighted by their error probability. While distinguishing between different error rates of different components in the circuit is straightforward, the factorization of the two-qubit noise channel into independent channels crucially relied on the symmetry between the different $P_i \otimes P_j$ terms. This suggests that biasing a particular two-qubit noise term would make the prefactor in Eq. (S1) non-symmetric and thus hinder the factorization of the channel. As a side note, we remark on a slightly non-intuitive feature in the conventional definition of the depolarizing channel: if we define it (as we do) as a random application of Paulis, complete depolarization (i.e. deterministically receiving the completely mixed state) corresponds to $\lambda = 3/4$ (single qubit depolarizing channel) or $\lambda = 15/16$ (two-qubit depolarizing channel), which shows that no term in the product inside Eq. (S4) becomes negative. Additionally, some works in the literature choose to not use a depolarizing noise for every location but rather put a bit-flip channel at the initialization and measurement locations. The two differ by a rescaling-factor of 2/3, since only two of the three Pauli errors lead to errors at initialization and readout (e.g. in the computational basis a Z acts trivially etc.).

II. DERIVATION OF THE CORRELATED DISORDERED INTERACTING CLASSICAL SPIN MODEL

The technique of the statistical mechanical mapping is used to construct a classical statistical Hamiltonian with quenched disorder for describing the error model of a quantum code. The mapping relies on the identification of the partition function of the Hamiltonian with the probability $\text{Pr}(\bar{E})$ of the class $\bar{E} = \{E'\}$ of errors E' that are equivalent up to the action of space-time equivalences to a reference error E . Several ways have been introduced for deriving this mapping [S2, S3]. Here we will follow mainly the approach of Ref. [S3].

Any error E of the repetition code is composed of the fundamental errors e_1, e_2, e_3 introduced in the main text that in turn are generated by the three error processes (i) single-qubit phase flip error on data qubits with probability p , (ii) measurement error with probability q , and (iii) single-qubit phase flip errors happening on the target qubit between two adjacent CNOT gates that trigger a correlated occurrence of a measurement error on one of the neighboring ancilla qubits with probability r .

The probabilities of the errors e_1, e_2, e_3 are easily calculated and are given by

$$\begin{aligned} \pi_0 &\equiv \text{Pr}(e_0) = (1 - p)(1 - q)(1 - r) + pqr, \\ \pi_1 &\equiv \text{Pr}(e_1) = p(1 - q)(1 - r) + rq(1 - p), \\ \pi_2 &\equiv \text{Pr}(e_2) = q(1 - p)(1 - r) + rp(1 - q), \\ \pi_3 &\equiv \text{Pr}(e_3) = pq(1 - r) + r(1 - p)(1 - q). \end{aligned} \quad (\text{S5})$$

where, for completeness, we added the probability of the trivial error e_0 that corresponds to the absence or the simultaneous presence of all of the three error processes.

In a section of the lattice in Fig. 1(c1) of the main text made only of a horizontal and a vertical link (shown also in Fig. S2), the probability of a generic event E composed by the errors e_j with $j = 0, 1, 2, 3$ can be written as

$$\text{Pr}(E) = \pi_0^{f_0(v,h)} \pi_1^{f_1(v,h)} \pi_2^{f_2(v,h)} \pi_3^{f_3(v,h)} \quad (\text{S6})$$

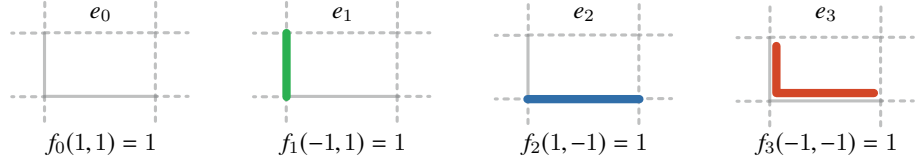


FIG. S2. Fundamental errors e_0, e_1, e_2, e_3 parametrized by two binary variables $v, h \in \{-1, +1\}$ for the vertical and horizontal links and four Boolean functions $f_j(v, h) \in \{0, 1\}$. The trivial error e_0 corresponds to $(v, h) = (1, 1)$ and the function f_0 satisfies $f_0(1, 1) = 1$. The error e_1 corresponds to $(v, h) = (-1, 1)$ and the function f_1 satisfies $f_1(-1, 1) = 1$. The error e_2 corresponds to $(v, h) = (1, -1)$ and the function f_2 satisfies $f_2(1, -1) = 1$. The error e_3 corresponds to $(v, h) = (-1, -1)$ and the function f_3 satisfies $f_3(-1, -1) = 1$. On all the other cases not shown in the figure, the functions $f_j(v, h)$ are zero.

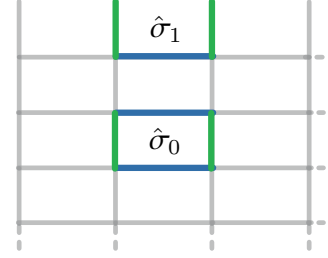


FIG. S3. The equivalence $\hat{\sigma}_0$ in the bulk and $\hat{\sigma}_1$ at the boundary of the space-time lattice. The equivalence $\hat{\sigma}_0$ is given by the combined action of two measurement errors on the ancilla qubits (horizontal blue links) preceded and followed by phase flip errors on the data qubit (vertical green links) adjacent to the ancilla qubits. The equivalence $\hat{\sigma}_1$ at the boundary is given by the combined action of one measurement error preceded by followed by phase flip errors on the data qubit.

where $v, h \in \{\pm 1\}$ are binary variables that take the negative value -1 if the horizontal (vertical) link belongs to the error E . The Boolean functions $f_j \in \{0, 1\}$ signal if e_j belongs to the error E and they satisfy $f_0(v = +1, h = +1) = f_1(v = -1, h = +1) = f_2(v = +1, h = -1) = f_3(v = -1, h = -1) = 1$, otherwise they are zero. From this, they can be written as

$$\begin{aligned} f_0(v, h) &= \frac{1}{4}(1 + h + v + vh), & f_1(v, h) &= \frac{1}{4}(1 + h - v - vh), \\ f_2(v, h) &= \frac{1}{4}(1 - h + v - vh), & f_3(v, h) &= \frac{1}{4}(1 - h - v + vh). \end{aligned} \quad (S7)$$

By substituting the Eqs. (S7) in Eq. (S6), the probability $\text{Pr}(E)$ can be written as

$$\text{Pr}(E) = \exp[-\beta H_E], \quad (S8)$$

where $H_E = -J_0 - J_1 h - J_2 v - J_3 v h$ is a noise Hamiltonian [S3] and the couplings J_0, J_1, J_2, J_3 satisfy

$$\begin{aligned} \beta J_0 &= \frac{1}{4} \log(\pi_0 \pi_1 \pi_2 \pi_3), & \beta J_1 &= \frac{1}{4} \log \frac{\pi_0 \pi_1}{\pi_2 \pi_3}, \\ \beta J_2 &= \frac{1}{4} \log \frac{\pi_0 \pi_2}{\pi_1 \pi_3}, & \beta J_3 &= \frac{1}{4} \log \frac{\pi_0 \pi_3}{\pi_1 \pi_2}. \end{aligned} \quad (S9)$$

These are the Nishimori conditions connecting the Hamiltonian H_E to the error model of Eq. (S5). The Hamiltonian H_E can be extended to the whole lattice by introducing binary variables $h_\ell, v_\ell \in \{\pm 1\}$ associated to each link ℓ of the lattice. The variables h_ℓ (v_ℓ) take the negative value -1 if the horizontal (vertical) link ℓ belongs to the error E . The Hamiltonian will then take the form

$$H_E = - \sum_{\ell} (J_0 + J_1 h_\ell + J_2 v_\ell + J_3 v_\ell h_\ell). \quad (S10)$$

The syndrome associated with the error E can also be generated by other error chains $E' = E\hat{\sigma}$ that differ from E by the action of the space-time equivalences $\hat{\sigma}$ that are trivial sequences of data-qubit errors and measurement errors that are not detected by the stabilizers. Figure S3 shows the lattice with two highlighted equivalences: $\hat{\sigma}_0$ and $\hat{\sigma}_1$ belonging to the bulk and the boundary of the lattice, respectively.

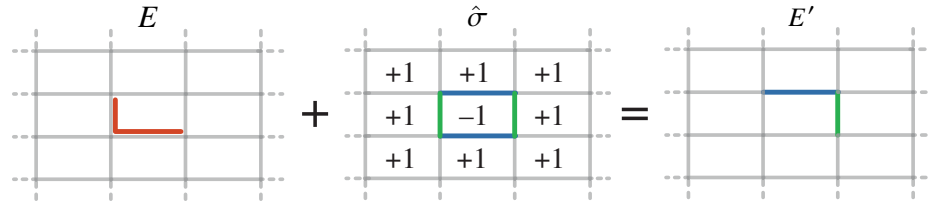


FIG. S4. Action of the equivalence $\hat{\sigma}$ on an error $E = e_3$ (red L-shaped link). The equivalence $\hat{\sigma}$ (central panel) is given by two data-qubit errors (vertical green links) and two measurement errors (horizontal blue links). On the lattice the action of σ is represented by a closed loop and it can be parametrized by a configuration of classical Ising spins $\{\sigma = \pm 1\}$ as explained in the text.

We can associate classical Ising spins $\{\sigma\}$ to each of the equivalences such that if a spin σ in this configuration is -1 , we are effectively considering the error $E' = E\hat{\sigma}$ that differs from the reference error E by the equivalence $\hat{\sigma}$ (for an example of an equivalence applied to an error E see Fig. S4). These Ising spins $\{\sigma\}$ can be associated to the plaquettes of the lattice in Fig. 1(c1) of the main text (see also Fig. S4). The data-qubit errors (green vertical links in Fig. S4) entering the equivalence $\hat{\sigma}$ are given by the vertical links ℓ of the lattice for which the product $\sigma_\ell\sigma_{\ell'} = -1$ where the equivalences $\sigma_\ell, \sigma_{\ell'}$ belong to the left and the right plaquettes w.r.t ℓ (Fig. S5(a)). Similarly, the measurement errors (blue horizontal links in Fig. S4) entering the equivalence $\hat{\sigma}$ are associated to the horizontal links ℓ of the lattice for which the product $\sigma_\ell\sigma_{\ell'} = -1$ where the equivalences $\sigma_\ell, \sigma_{\ell'}$ belong to the top and the bottom plaquettes w.r.t. ℓ (Fig. S5(b)).

The probability $\text{Pr}(E')$ of the error E' can also be written as $\text{Pr}(E') = \exp[-\beta H_{E'}]$ where in the noise Hamiltonian $H_{E'} = -\sum_\ell (J_0 + J_1 h'_\ell + J_2 v'_\ell + J_3 v'_\ell h'_\ell)$ the binary parameters h'_ℓ and v'_ℓ defining the error E' are fixed by the parameters h_ℓ and v_ℓ of E and by the equivalence σ as follows:

- for a vertical link ℓ , $v'_\ell = v_\ell \sigma_\ell \sigma_{\ell'}$ where the equivalences $\sigma_\ell, \sigma_{\ell'}$ are on the left and on the right of ℓ (Fig. S5(a));
- for a horizontal link ℓ , h'_ℓ is given by $h'_\ell = h_\ell \sigma_\ell \sigma_{\ell'}$ where the equivalences σ_ℓ and $\sigma_{\ell'}$ are on top and at the bottom of ℓ (Fig. S5(b)).

Substituting the variables h'_ℓ and v'_ℓ in the Hamiltonian $H_{E'}$ allows us to compute the probability $\text{Pr}(\bar{E})$ of the class $\bar{E} = \{E'\}$ composed by errors E' that are equivalent up to the action of equivalences to a reference error E as

$$\text{Pr}(\bar{E}) = \sum_{\{\hat{\sigma}\}} \text{Pr}(E\hat{\sigma}) = \sum_{\{\sigma\}} \exp[-\beta H_E(\sigma)], \quad (\text{S11})$$

where

$$H_E(\sigma) = - \sum_{\ell \leftrightarrow \ell'} J_1 h_\ell \sigma_\ell \sigma_{\ell'} - \sum_{\ell \leftrightarrow \ell'} J_2 v_\ell \sigma_\ell \sigma_{\ell'} - \sum_{\ell \leftrightarrow \ell'} J_3 h_\ell v_\ell \sigma_\ell \sigma_{\ell'} \quad (\text{S12})$$

is the Ising Hamiltonian with correlated disorder of the main text and we have neglected the unimportant additive constant J_0 . The couplings J_1, J_2, J_3 and the inverse temperature β are fixed from the error model describing E by the Nishimori conditions previously obtained (see Eq. (S9)). The type of interactions (ferromagnetic or antiferromagnetic) is given by the signs of v_ℓ and h_ℓ that are fixed by the reference error E . In the first sum of the r.h.s. of Eq. (S12), σ_ℓ and $\sigma_{\ell'}$ are the spins horizontally adjacent to the link ℓ (e.g. spins σ_1 and σ_2 in Fig. 1(c1) of the main text); in the second sum, σ_ℓ and $\sigma_{\ell'}$ are the spins vertically adjacent to the link ℓ (e.g. spins σ_3 and σ_4 in Fig. 1(c1) of the main text); in the third sum, σ_ℓ and $\sigma_{\ell'}$ are the two spins adjacent to the two arms of the L-shaped error e_3 (e.g. spins σ_5 and σ_6 in Fig. 1(c1) of the main text). Equation (S11) shows that the probability $\text{Pr}(\bar{E})$ of the class \bar{E} can be written as the partition function $\mathcal{Z}_E = \sum_{\{\sigma\}} \exp[-\beta H_E(\sigma)]$ of a statistical mechanical Hamiltonian $H_E(\sigma)$. Given an error E and the equivalences, one can also define the two classes $\overline{EO_L}$ for each logical operator $O_L = Z_L, X_L$ and compute the relative probabilities $\text{Pr}(\overline{EO_L})$ by the statistical mechanical mapping. Comparing the partition functions $\mathcal{Z}_E = \text{Pr}(\bar{E})$ and $\mathcal{Z}_{EO_L} = \text{Pr}(\overline{EO_L})$ allows us to determine if the error is correctable which occurs if $\mathcal{Z}_E > \mathcal{Z}_{EO_L}$ for any logical operator. This condition can be related to a phase transition in the statistical Hamiltonian $H_E(\sigma)$ since the free energy cost Δ_L (averaged on the quenched disorder and in the thermodynamic limit) associated to the partition functions defined as $\beta\Delta_L = -\log(\mathcal{Z}_{EO_L}/\mathcal{Z}_E)$ satisfies $\Delta_L \rightarrow \infty$ in the correctable phase, while $\Delta_L \rightarrow 0$ in the non-correctable phase [S3].

III. MONTE-CARLO SIMULATION STUDY OF THE PHASE DIAGRAM

In this section we present the details on the numerical simulations of the Hamiltonian $H_E(\sigma)$. In particular, we describe how we choose the couplings J_1, J_2, J_3 of $H_E(\sigma)$ and the methods for obtaining the phase transition points.

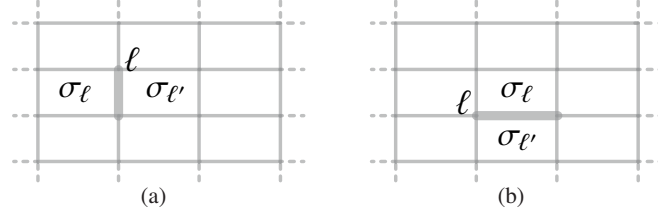


FIG. S5. Parametrization of the equivalences and the error E' . For the equivalences: Given an Ising spin configuration $\{\sigma\}$ where each spin is associated to the plaquette of the lattice (see Fig. S4 central panel), (a) a data-qubit error occurring on the vertical link ℓ enters the equivalence $\hat{\sigma}$ if the product $\sigma_\ell \sigma_{\ell'} = -1$ where the equivalences $\sigma_\ell, \sigma_{\ell'}$ are on the left and on the right of ℓ . (b) Measurement errors occurring on the horizontal link enters the equivalence $\hat{\sigma}$ if the product $\sigma_\ell \sigma_{\ell'} = -1$ where the equivalences $\sigma_\ell, \sigma_{\ell'}$ are at the top and at the bottom of ℓ . For the error E' : given a reference error E described by the binary variables v_ℓ and h_ℓ and the equivalences $\hat{\sigma}$, the error E' equivalent to E up to $\hat{\sigma}$ is parametrized by v'_ℓ and h'_ℓ with (a) $v'_\ell = v_\ell \sigma_\ell \sigma_{\ell'}$ where the equivalences $\sigma_\ell, \sigma_{\ell'}$ are on the left and on the right of ℓ and (b) for a horizontal link ℓ , h'_ℓ is given by $h'_\ell = h_\ell \sigma_\ell \sigma_{\ell'}$ where the equivalences σ_ℓ and $\sigma_{\ell'}$ are on top and at the bottom of ℓ .

z_p	z_q	z_r	Errors		Couplings		
			v_ℓ	h_ℓ	$J_1 h_\ell$	$J_2 v_\ell$	$J_3 v_\ell h_\ell$
+1	+1	+1	+1	+1	F	F	F
+1	+1	-1	-1	-1	AF	AF	F
+1	-1	+1	+1	-1	AF	F	AF
+1	-1	-1	-1	+1	F	AF	AF
-1	+1	+1	-1	+1	F	AF	AF
-1	+1	-1	+1	-1	AF	F	AF
-1	-1	+1	-1	-1	AF	AF	F
-1	-1	-1	+1	+1	F	F	F

TABLE I. The binary variables z_p, z_q, z_r , drawn randomly with probabilities p, q, r , represent the fundamental errors and fix the sign of the variables v_ℓ, h_ℓ and thus of the couplings (ferromagnetic (F) or antiferromagnetic (AF)) of the noise Hamiltonian of the random bond Ising model Eq. (S12).

A. Couplings of the random bond-Ising model

The Hamiltonian of Eq. (S12) that we analyse corresponds to a random-bond Ising model on a triangular lattice with couplings J_1, J_2 and J_3 (see Fig. 1(c2) of the main text). Relative ratio of these couplings are fixed by the Nishimori conditions (see Eq. (S9)) while the type of interactions (ferromagnetic or antiferromagnetic) is assigned by drawing three random binary variables $z_p, z_q, z_r \in \{\pm 1\}$ with probability p, q, r for each link of the triangular lattice. These variables take the negative sign if one of fundamental processes (data-qubit error, measurement error, correlated error) is present in the reference error E . Therefore, they fix the signs of the variables v_ℓ and h_ℓ and thus of the couplings entering the Hamiltonian of Eq. (S12) according to Table I.

B. Finite-size scaling and transition points

In order to locate the phase transition points we employ a finite-size scaling procedure. For a finite lattice with $L \times L$ sites ($L = 16, 24$ and 32), we define the Fourier transform of the spin correlation function $\langle \sigma_0 \sigma_{\vec{x}} \rangle$ as

$$\hat{G}_L(\vec{k}) = \sum_{\vec{x}} \langle \sigma_0 \sigma_{\vec{x}} \rangle_L e^{i\vec{k} \cdot \vec{x}} \quad (\text{S13})$$

and we extract the correlation length ξ_L in the unit of lattice spacing from

$$\xi_L = \frac{1}{2 \sin(q_{\min}/2)} \sqrt{\frac{\langle \hat{G}_L(0) \rangle_{\text{av}}}{\langle \hat{G}_L(q_{\min}) \rangle_{\text{av}}} - 1} \quad (\text{S14})$$

where $q_{\min} = (2\pi/L, 0)$. The brackets $\langle \dots \rangle_{\text{av}}$ denote averages over the quenched disorder distribution (in addition to the thermal average). Near the critical temperature T_c , the correlation length ξ_L is expected to obey a scaling relation [S4] of the form $\xi_L/L \sim f(L^{1/\nu}(T - T_c))$, where f is an unknown scaling function and ν is the critical exponent related to the correlation length. Therefore, at the critical temperature T_c , the quantity ξ_L/L becomes independent of the temperature and T_c can be found by

case	p	T_c	N_{met}
(I) $p = q = 2r$	0.001	3.86(2)	800
	0.020	3.72(2)	800
	0.040	3.38(2)	800
	0.060	2.93(2)	800
	0.080	2.00(2)	800
	0.090	1.43(2)	800
(II) $p = q = r$	0.000	3.64(2)	800
	0.020	3.21(2)	800
	0.040	2.74(2)	800
	0.060	2.19(2)	800
	0.070	1.67(2)	800
(III) $p = q = r/2$	0.001	3.38(2)	800
	0.020	2.75(2)	800
	0.030	2.44(2)	800
	0.040	2.07(2)	800
	0.045	1.80(2)	800
(IV) $p = q, r = 0$	0.000	2.266(2)	800
	0.060	1.760(5)	800
	0.080	1.565(5)	800
	0.100	1.32(1)	800
	0.105	1.16(1)	800
	0.110	0.93(5)	8000

TABLE II. Critical temperatures T_c for the different cases (I)-(IV) of quenched disorder from the Monte Carlo simulations. The columns report the case analyzed, the quenched disorder probability p , the corresponding critical temperature T_c obtained by performing N_{met} Metropolis steps.

case	largest p showing a critical temperature	smallest p not showing a critical temperature
(I) $p = q = 2r$	0.090	0.095
(II) $p = q = r$	0.070	0.075
(III) $p = q = r/2$	0.045	0.050
(IV) $p = q, r = 0$	0.110	0.115

TABLE III. Lower and upper bounds of the probability p between which the system exhibits a critical temperature for the cases (I)-(IV). The threshold probabilities and the associated errors shown in Fig. 3 of the main text for the statistical mechanics model are estimated by the mean and the deviation of these bounds for p .

locating the temperature at which the lines representing ξ_L/L for different L intersect. Some examples of the comparisons of ξ_L/L are given in Fig. S6 for the case $p = q = 2r$. In each figures, the vertical line indicates the temperature at which ξ_L/L cross for three different lattice sizes L . The figure without the vertical line shows the case in which there is no phase transition.

For computing the spin correlation function and thus the correlation length we use the standard Metropolis algorithm [S5] interspersed with parallel tempering between adjacent temperatures to allow efficient sampling of the low temperature phase [S6, S7]. Moreover, for a given quenched disorder distribution, the spin configurations are swapped after $N_{\text{met}} = 800$ Metropolis steps following parallel tempering algorithm (except the data point for $p = q, r = 0$ with $p = 0.11$ (open blue circle in Fig. 2 of the main text) where $N_{\text{met}} = 8000$ Metropolis steps are performed). Metropolis steps/spin-swap combination are repeated 10000 times. The spin correlation function is measured during the Metropolis steps. Averages are taken over the Metropolis steps and then these averages serve as one of the jack-knife bins used to determine the statistical error. We use 250 different quenched disorder samples to compute the average of the correlation length over the disorder distribution. Table II lists the details of the numerics: for every case shown in Fig. 2 of the main text, when the probability p is fixed to the values reported in the second column of the table, we found the critical temperatures reported in the third column when the simulations are carried with a number of metropolis step N_{met} .

For assessing whether the random bond Ising model has thermalized we perform additional checks near the quenched probabilities at which the thermal transition crosses the Nishimori lines (Fig. 2 of the main text). In Fig. S7, we compare the effects of increasing the Metropolis steps between parallel tempering spin-swap steps. Comparing the two top panels of Fig. S7, we observe that there is no noticeable difference in the crossing of the lines ξ_L/L when the number of Metropolis steps is increased from 800 (panel (a)) to 8000 (panel (b)) for the probability $p = q = r = 0.070$. On the other hand, the comparison of the two bottom panels in Fig. S7 ($p = q = r = 0.075$) shows that the crossing of ξ_L/L for the three different lattice sizes, which seems to suggest a phase transition in panel (c) for 800 Metropolis steps, almost disappears for 8000 Metropolis steps (panel (d)) and the lines of ξ_L/L overlap for all the temperatures $T \lesssim 1.35$. Therefore we conclude that there is no transition at the quenched

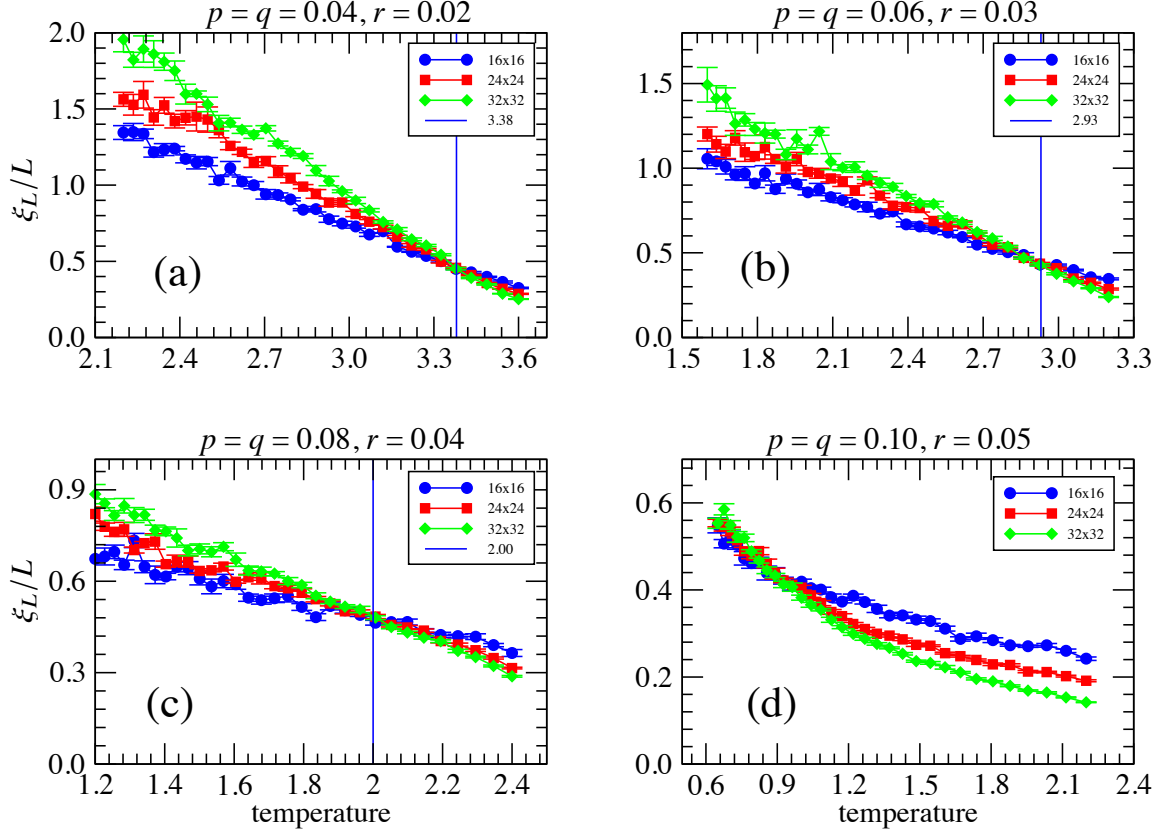


FIG. S6. Critical temperatures from finite size scaling. The critical temperatures are found by locating the points where the lines representing the quantities ξ_L/L cross each other for different systems sizes L . Examples of the occurrence of a phase transition are shown in (a) for $p = q = 0.04, r = 0.02$, in (b) for $p = q = 0.06, r = 0.03$, in (c) for $p = q = 0.08, r = 0.04$. If it is not possible to identify a temperature where the lines with the quantities ξ_L/L cross, the transition does not occur. This is shown in panel (d) for $p = q = 0.10, r = 0.05$.

disorder probability $p = q = r = 0.075$ and the threshold probability should be larger than 0.070 but smaller than 0.075.

In Table III, we list the largest p 's at which MC simulations (run for $N_{\text{met}} = 8000$) show a phase transition and the smallest p 's at which MC simulations do not show a phase transition for the cases (I)-(IV). Figure 3 in the main text is produced with these data. The central value of these two p 's is taken as the estimated threshold probability and a half of the difference is given as the error estimate. A more precise determination of the threshold probability will require even longer Metropolis updates between parallel tempering steps.

IV. MINIMUM-WEIGHT-PERFECT-MATCHING DECODING

To motivate this decoding strategy, observe that the probability of some error pattern E consisting of n_i errors of the i -th type, where $i = p, q$ or r) is proportional to

$$p(E) \propto \left(\frac{p}{1-p} \right)^{n_p(E)} \left(\frac{q}{1-q} \right)^{n_q(E)} \left(\frac{r}{1-r} \right)^{n_r(E)}. \quad (\text{S15})$$

Given some observed collection of stabilizer measurement outcomes (the syndrome), repairing that syndrome amounts to finding a configuration of errors where every violated syndrome (a defect) is the endpoint of one error string, an assignment known as a (perfect) matching in graph theory (Fig. S8). Now Eq. (S15) implies that finding the most likely among all these is equivalent to finding an error configuration with the lowest weight $w_{\text{tot}} = -\log(p(E)) = n_p w_p + n_q w_q + n_r w_r$, hence *minimum weight* perfect matching. By creating a graph with all defects as vertices and the weight between every two nodes given by the number of error locations times error type weight ($w_p = -\log \frac{p}{1-p}$ etc.) between the respective stabilizers, this is what is solved by the above mentioned Blossom algorithm (implemented e.g. in [S8]). As a side remark, we note that the QEC code at hand does have a boundary, i.e. error strings extending to a boundary qubit only create a single defect, which is not immediately amenable to

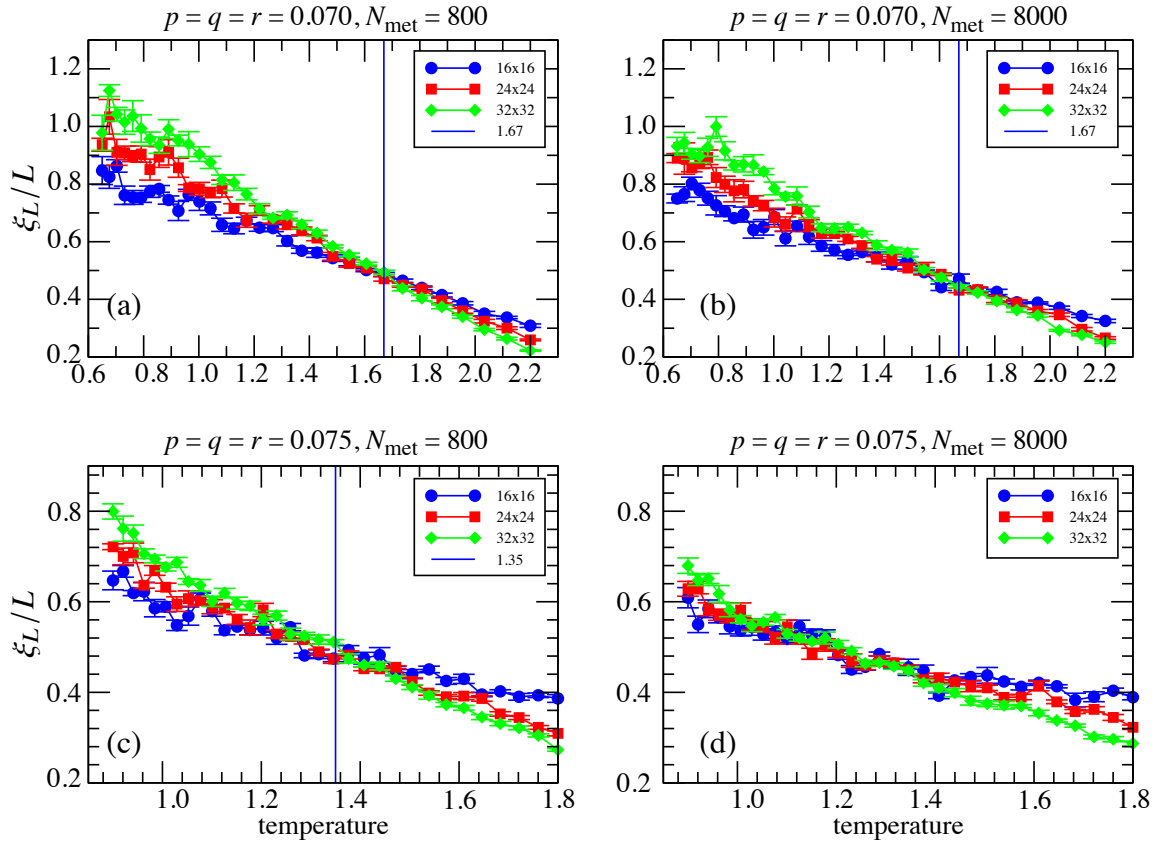


FIG. S7. Effect of increasing the Metropolis steps. The quantity ξ_L/L computed with (a) 800 Metropolis steps and (b) 8000 Metropolis steps is shown for $p = q = r = 0.07$ before the Nishimori line is crossed. In this case a transition is identified at a temperature $T_c = 1.67$. When instead $p = q = r = 0.075$ after the Nishimori line is crossed, a transition at $T_c = 1.35$ seems to appear when ξ_L/L is computed with 800 Metropolis steps (panel (c)). However, when we compute ξ_L/L with 8000 Metropolis steps (d) the lines do not cross any more and overlap for the temperature less than 1.35. This implies that a transition does not occur when $p = q = r = 0.075$.

the above but can be incorporated by creating a copy of the matching graph with weights set to zero and then putting an edge between every defect and its virtual partner with the corresponding weight of matching to the code boundary [S9]. Due to the addition of r -type edges the calculation of weights going into the matching problem has to be adapted as well. While in general we would have to compute the shortest path on a triangular lattice with the three types of edges being weighted respectively, which can be done by a Dijkstra-type algorithm, we can make a vast simplification by observing that the shortest path between any two vertices in our setting can always be found by considering error patterns consisting of two types of errors only. To see this, observe that any single edge in a certain path can be replaced by the other two edges in the triangle, which are hence of the other two types, e.g. a particular r -edge can be circumvented by moving across the neighboring p - and q -edge. Furthermore all vertices are connected to at least one edge of each type and the weights are globally the same (up to the edge type). Let us assume that $w_r < w_p + w_q$ (if this was not the case the metric would not change compared to the case without r -edges). Now the two possible cases are that either $w_r + w_p < w_q$ or $w_r + w_p > w_q$. In the former case, we replace all q -moves by the same amount of r - and p - moves, in the latter case we do the opposite and replace all p -moves by q - and r -moves, which shows that given a path, we can always find a path of lower weight by eliminating one of the edge types. In the borderline case $w_r + w_p = w_q$ both replacements are admissible, such that the statement holds that we can eliminate one edge type (see Fig. S9). This shows that a minimum weight path between any two vertices necessarily lies on one of the three sublattices and the path weight on a sublattice is given by the Manhattan distance on the respective sublattice:

$$wt(s_1, s_2) = \min \begin{cases} \|s_1 - s_2\|_1^{pq} \\ \|s_1 - s_2\|_1^{pr} \\ \|s_1 - s_2\|_1^{qr} \end{cases} . \quad (S16)$$

Here the two superscript labels indicate the sublattice of the triangular lattice, that consists of the two types of edges. In the pq case this is just the regular Manhattan distance, counting the number of p and q edges between the two vertices at hand. In case

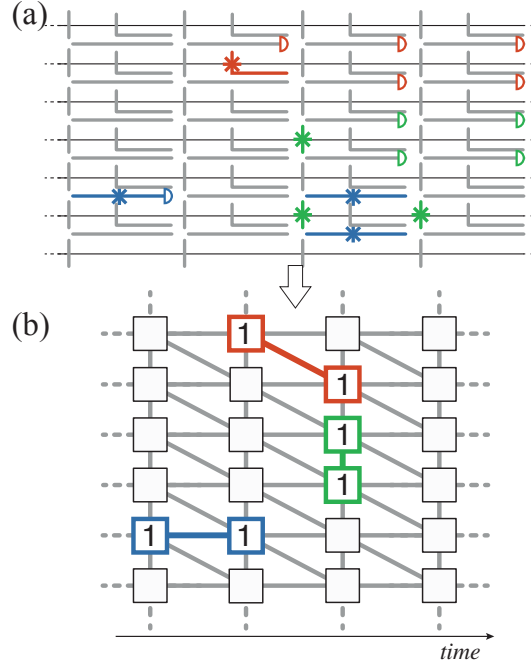


FIG. S8. (a) Example of an error graph generated by physical errors. Positions where qubit, measurement and correlated data phase-flip and measurement errors can happen are represented by vertical, horizontal and L-shaped edges, respectively. Colored links represent occurred error events while colored semicircles represent the ancilla qubits triggered by an error event. From this graph we derive syndrome volume which is the input for the MWPM decoder. (b) Syndrome volume graph derived by the error graph in (a). The boxes labeled with 1s represent defects, i.e. ancilla qubits where the measurement outcome differs from the previous round of measurements. The colored diagonal red, vertical green and horizontal edges represent a matching of the defects.

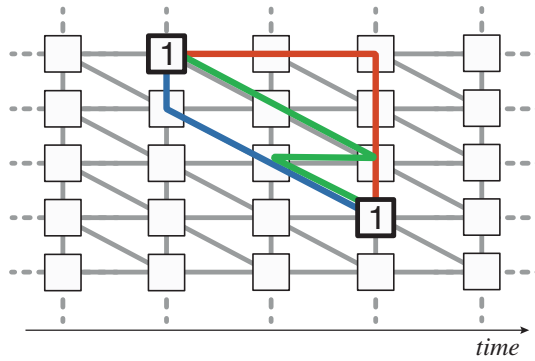


FIG. S9. Simplification in computing the distance of two defects (boxes labeled with 1s) in the triangular lattice. Depending on the values of the weights w_p, w_q, w_r the shortest path between any two vertices can always be found by considering error patterns consisting of two types of errors only. If $w_r > w_p + w_q$ (pq case) the shortest path is the regular Manhattan distance of the square lattice, counting the number of p and q edges between the two defects (red path). If $w_r + w_p < w_q$ (pr case) the shortest path is composed by only p and r edges (blue path). Similarly, if $w_r + w_p > w_q$ (qr case) the shortest path is composed by only q and r (green path).

of pr and qr this is the Manhattan distance on a skewed square lattice, but by simply rotating the basis vectors we can still use the Euclidean position vectors to compute the Manhattan distance on the respective sublattices. The weight function assigning the weight between any two defects then simply takes the minimum over the three weighted Manhattan distances. Having assigned the edge weights, we can then solve the minimum weight matching problem, which amounts to finding the most likely collection of errors explaining the observed syndrome in a trial run, from which we can therefore deduce the recovery operation we should apply to the code (or in which way we should update the “Pauli frame”). The figure of merit we are after is the logical error rate, the probability that the decoding strategy fails. In order to cleanly decide in our simulation whether a logical error happened or did not happen, we initialize a perfect codeword, we then simulate d subsequent QEC-cycles, each consisting of injecting phase-flip errors with probability p on each data qubit followed by a noisy syndrome extraction (the syndrome bit

being flipped with probability q). We furthermore inject the third error type needed, namely a correlated flip of the data-qubit accompanied by a flip of one of the syndrome measurement outcomes adjacent to it (depending on the order of the two-qubit gates this deterministically happens on the syndrome bit sitting either to the left or to the right of the data qubit). This type of error is injected with probability r . In order to make sure that we can declare the binary outcome of the trial run logical error/no logical error, we let the final measurement be perfect, i.e. in the final round the syndrome bits never flip (with q or r). The final measurement being perfect ensures that matching up all defects will with certainty put the data qubits back into a code state. The simulation results are shown in Fig. S10.

[S1] D. Greenbaum, “Introduction to quantum gate set tomography,” (2015), [arXiv:1509.02921 \[quant-ph\]](https://arxiv.org/abs/1509.02921).

[S2] E. Dennis, A. Kitaev, A. Landahl, and J. Preskill, *J. Math. Phys.* **43**, 4452 (2002).

[S3] C. T. Chubb and S. T. Flammia, “Statistical mechanical models for quantum codes with correlated noise,” (2019), [arXiv:1809.10704 \[quant-ph\]](https://arxiv.org/abs/1809.10704).

[S4] M. Palassini and S. Caracciolo, *Phys. Rev. Lett.* **82**, 5128 (1999).

[S5] N. Metropolis, A. W. Rosenbluth, M. N. Rosenbluth, A. H. Teller, and E. Teller, *The Journal of Chemical Physics* **21**, 1087 (1953).

[S6] R. H. Swendsen and J.-S. Wang, *Phys. Rev. Lett.* **57**, 2607 (1986).

[S7] D. J. Earl and M. W. Deem, *Phys. Chem. Chem. Phys.* **7**, 3910 (2005).

[S8] A. Hagberg, D. A. Schult, and P. J. Swart, in *Proceedings of the 7th Python in Science Conference*, edited by G. Varoquaux, T. Vaught, and J. Millman (Pasadena, CA USA, 2008) pp. 11 – 15.

[S9] D. Wang, A. Fowler, A. Stephens, and L. Hollenberg, *Quant. Inf. Comp* **10**, 456 (2010).

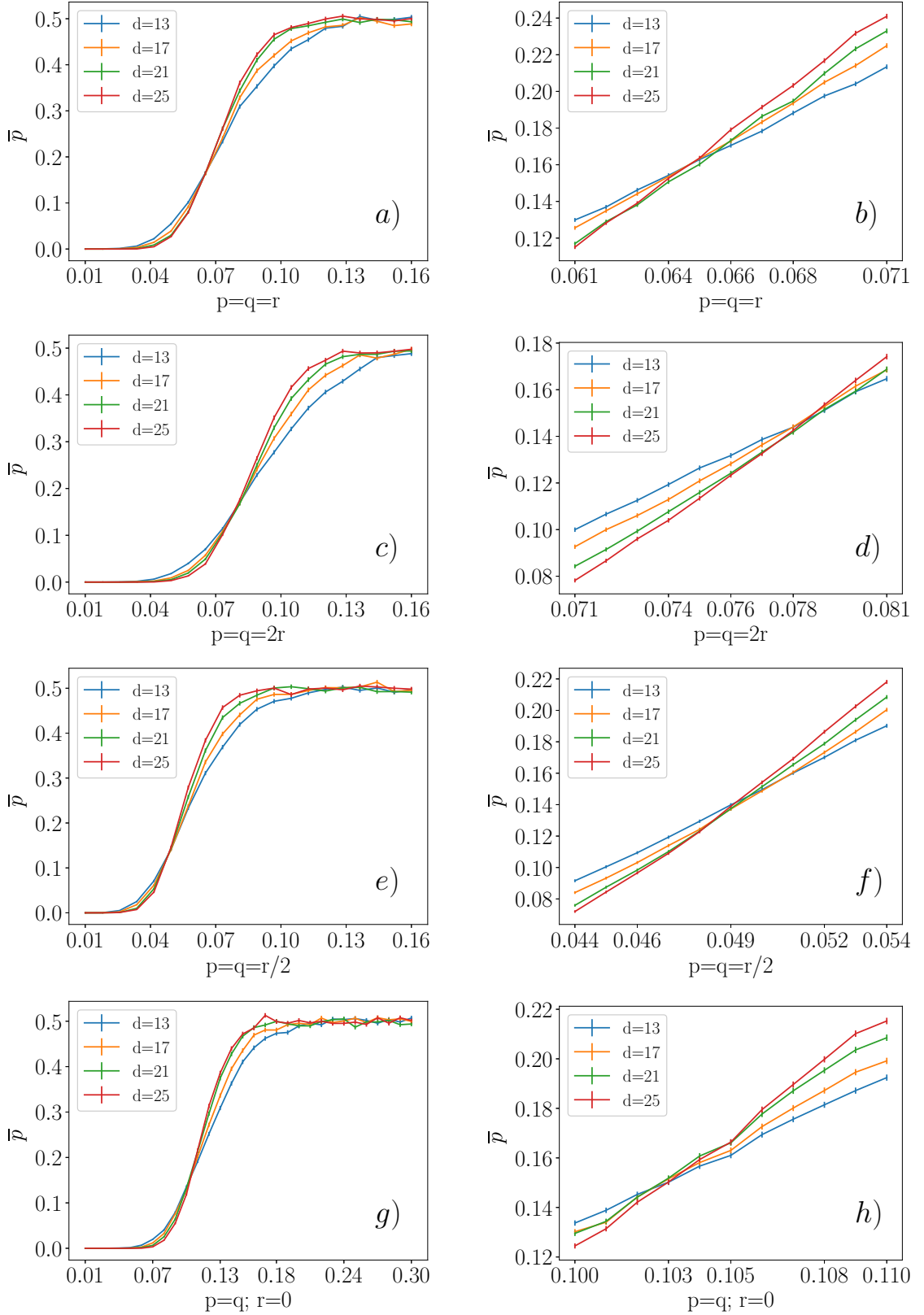


FIG. S10. The logical error rate obtained with the minimum weight perfect matching decoder on the triangular syndrome lattice. Left column is a broad sweep, right column is a closeup around the transition point. We plot the average logical error rate as a function of the input error rates p, q , and r . Shown are the three cases $p = q = r$ in a)+b), $p = q = 2r$ in c)+d), $p = q = r/2$ in e)+f) and $p = q, r = 0$ in g)+h). On the left for the broader scan, we use 10^4 samples, data points in the right column are averaged over 10^5 samples. In each case, we observe a transition from error suppression to error enhancement with increasing error rate. This transition is signified by the behavior of the logical error rate when increasing the code size (the distance d): for small p , increasing the distance leads to a suppression of the logical error rate, whereas for error rates beyond an inflection point increasing the code size instead leads to an increased logical error rate. We estimate the threshold from the region where we can not distinguish the logical error rates within errorbars.